

Efficient calculation of \mathbf{k} -integrated electron energy loss spectra: Application to monolayers of MoS₂, hBN, and graphene

Stefan Rost ^{1,2}, Stefan Blügel ^{1,2} and Christoph Friedrich ^{1,*}

¹*Peter Grünberg Institut and Institute for Advanced Simulation, Forschungszentrum Jülich and JARA, 52425 Jülich, Germany*

²*Department of Physics, RWTH Aachen University, 52056 Aachen, Germany*



(Received 5 April 2022; revised 23 January 2023; accepted 26 January 2023; published 21 February 2023)

The theoretical scattering cross section of electron energy loss spectroscopy (EELS) is essentially given by $-\text{Im} \varepsilon^{-1}(\mathbf{k}, \omega)$ with the energy loss $\hbar\omega$ and the momentum transfer $\hbar\mathbf{k}$. The macroscopic dielectric function $\varepsilon(\mathbf{k}, \omega)$ can be calculated from first principles using time-dependent density-functional theory. However, experimental EELS measurements have a finite \mathbf{k} resolution or, when operated in spatial resolution mode, yield a \mathbf{k} -integrated loss spectrum, which deviates significantly from EEL spectra calculated for specific \mathbf{k} momenta. On the other hand, integrating the theoretical spectra over \mathbf{k} is complicated by the fact that the integrand varies over several (typically six) orders of magnitude around $k = 0$. In this article, we present a stable technique for integrating EEL spectra over an adjustable range of momentum transfers. The important region around $k = 0$, where the integrand is nearly divergent, is treated partially analytically, allowing an analytic integration of the near divergence. The scheme is applied to three prototypical two-dimensional systems: monolayers of MoS₂ (semiconductor), hexagonal BN (insulator), and graphene (semimetal). Here, we are confronted with the added difficulty that the long-range Coulomb interaction leads to a very slow supercell (vacuum size) convergence. We address this difficulty by employing an extrapolation scheme, enabling an efficient reduction of the supercell size and thus a considerable speedup in computation time. The calculated \mathbf{k} -integrated spectra are in very favorable agreement with experimental EEL spectra.

DOI: [10.1103/PhysRevB.107.085132](https://doi.org/10.1103/PhysRevB.107.085132)

I. INTRODUCTION

In electron energy loss spectroscopy (EELS) [1,2], a beam of electrons passes through a thin sample. By interacting with the electrons and ions in the sample material, the electrons can lose energy and may be deflected from the direction of incidence in a way that is characteristic of the medium. The energy loss, measured in the form of a spectrum, contains a wealth of information about the excitation properties of the sample material, combined with the ability of atomic resolution using scanning transmission electron microscopy (STEM) [3].

Transmission EELS measurements can be performed in spatial and momentum resolution. Due to the Heisenberg uncertainty principle, improving either of the two is always at the expense of the other [4]. To measure the momentum, one places the electron detector at an angle from vertical incidence, which allows the lateral momentum transfer of the scattering process to be recorded together with the loss spectrum. When performing an EELS experiment without special focus on the momentum resolution, on the other hand, a large aperture is used in the experimental setup so that multiple momentum transfers are included in the loss spectrum [5]. For spatial resolution, a pixelated detector is used recording a spectrum at each pixel in real space. We note that an averaging over a region in reciprocal space may be needed also in the

momentum resolution mode, as the resolution in momentum is strongly limited by the experimental setup, typically to 0.1 \AA^{-1} [6].

On the theoretical side, it has been known for a long time [7,8] that electron energy loss spectra can be obtained from the imaginary part of the inverse macroscopic dielectric function $-\text{Im} \varepsilon^{-1}(\mathbf{k}, \omega)$, where $\hbar\omega$ is the energy loss and $\hbar\mathbf{k}$ is the momentum transfer. The macroscopic dielectric function can be calculated reliably with its full \mathbf{k} and ω dependence from time-dependent density-functional theory (TDDFT) or, if the exchange-correlation kernel is neglected, from the random-phase approximation.

Ab initio theoretical calculations can serve as an important tool to interpret the loss spectra measured in experiment, for example, to relate the spatially resolved loss spectra to particular atomic arrangements at the position of the beam focus. With all ingredients of the theoretical scattering cross section known in principle, it seems straightforward to carry out the necessary \mathbf{k} integrations of the loss spectra numerically. However, as a matter of fact, a reliable integration technique is still missing, arguably due to the fact that the integrand varies over several orders of magnitude around $k = 0$ for typical experimental electron velocities of 30 to 300 keV (corresponding to 30%–80% of the velocity of light). We fill this gap by presenting a reliable integration scheme, in which the integrand is written as two terms in the important region around $k = 0$, an analytic one and the rest. The (near) divergence of the integrand is confined to the analytic term, which can be integrated straightforwardly. The rest is

*c.friedrich@fz-juelich.de

nondivergent and shows a smooth behavior, enabling a numerical integration on a relatively coarse \mathbf{k} grid.

We apply the integration scheme to monolayers of prototypical two-dimensional materials: semiconducting MoS₂, insulating hexagonal boron nitride, and semimetallic graphene. Focus is laid on MoS₂, a member of the family of transition metal dichalcogenides, which has attracted a lot of attention in recent years due to its remarkable electronic, optoelectronic, spintronic, and valleytronic properties.

Most electronic-structure codes rely on periodic boundary conditions. However, a monolayer is infinite only in two dimensions but finite in the third. This difficulty is usually met by introducing supercells, i.e., large three-dimensional unit cells, that contain additional several nanometers thick vacuum separating the monolayers to reduce the unwanted layer-layer interaction. The larger the vacuum size (the supercell), the better the layers are decoupled.

The drawback is, of course, that large supercells are computationally demanding. This is particularly problematic in linear response theory, where the long-range Coulomb interaction can lead to very slow convergence with respect to the supercell size, and even more so in a situation where the unit cell is also large in the other two directions. Monolayers with defects are such a case. For example, defects in transition-metal dichalcogenides are of current interest, as they can trap excitons, which facilitate single-photon emission [9,10]. Especially for small or vanishing momentum transfers, calculations can become prohibitively expensive in this case.

A possible solution is to artificially truncate the Coulomb interaction in the out-of-plane direction [11], thus effectively decoupling the layers and eliminating the unwanted interlayer screening. However, this technique has been shown to lead to bad \mathbf{k} -point convergence [12,13]. In another approach, image-charge models are employed to subtract screening effects of the repeated slabs [14]. Tancogne-Dejean [15] and coworkers formulated a selected- G approach, which is based on a particular choice of plane waves (\mathbf{G} vectors) in the basis for the dielectric function and which was recently applied to EELS [16].

We solve the problem alternatively by employing a supercell extrapolation scheme, which was derived in Ref. [17] for the investigation of coupled electronic-lattice motion in 2D systems. We put it here to good use for our \mathbf{k} -integration algorithm applied to monolayers. In this scheme, one makes use of a mixed representation in reciprocal space (parallel to the layers) and real space (perpendicular to the layers). In this way, it is possible to separate the total density response into intra- and interlayer parts. One can then take the supercell limit (infinite layer distance) and so derive an extrapolation formula for the dielectric function. This formula turns out to significantly reduce the necessary vacuum size needed for convergence, thus strongly alleviating the computational burden.

The paper is organized as follows. In Sec. II, we recapitulate the theoretical derivation of the differential scattering cross section of EELS. In Sec. III, the integration over the momentum transfers is discussed and an integration technique is formulated. The integrand contains the \mathbf{k} and ω dependent dielectric function, which we calculate from first principles using the random-phase approximation as explained in

Sec. IV. Section V deals with the supercell convergence, which is particularly slow for small momentum transfers. The extrapolation formula, which accelerates the supercell convergence significantly, is introduced and discussed in Sec. VI. A short derivation is deferred to the Appendix. In Sec. VII, we discuss details of the calculations. Illustrative results are presented in Sec. VIII and compared to experimental spectra. Finally, we give a summary in Sec. IX.

II. ELECTRON ENERGY LOSS SPECTRUM

We briefly recapitulate the theoretical derivation of the scattering cross section of EELS. We choose here a semiclassical derivation [2], in which the relevant quantities have a simple physical interpretation. (See Ref. [18] for a fully quantum mechanical derivation.) The electron beam given by the current $\mathbf{j}(\mathbf{r}, t)$ experiences a decelerating field $\mathbf{E}(\mathbf{r}, t)$ created by the electrons of the material. The loss of electric power per unit volume at point \mathbf{r} and time t is given by

$$L(\mathbf{r}, t) = \mathbf{E}(\mathbf{r}, t)\mathbf{j}(\mathbf{r}, t). \quad (1)$$

We consider an electron beam at normal incidence. The coordinate system is oriented such that x and y axes are parallel to the sample slab, so the beam electrons are traveling in the z direction. The energy loss per unit path length is $w(z) = \int dx dy \int dt L(\mathbf{r}, t)$. Fourier-transforming $t \rightarrow \omega$ and $x, y \rightarrow \mathbf{k}_{\parallel}$ yields

$$w(z) = \frac{1}{8\pi^3} \int d^2k_{\parallel} \int_0^{\infty} d\omega [\mathbf{E}^*(\mathbf{k}_{\parallel}, z; \omega)\mathbf{j}(\mathbf{k}_{\parallel}, z; \omega) + \text{c.c.}]. \quad (2)$$

The loss per unit length can also be expressed with the differential scattering cross section

$$w(z) = \int d^2k_{\parallel} \int_0^{\infty} d\omega \hbar\omega \frac{\partial^3 P}{\partial^2 k_{\parallel} \partial \omega}, \quad (3)$$

giving

$$\frac{\partial^3 P}{\partial^2 k_{\parallel} \partial \omega} = \frac{1}{8\pi^3 \hbar\omega} [\mathbf{E}^*(\mathbf{k}_{\parallel}, z; \omega)\mathbf{j}(\mathbf{k}_{\parallel}, z; \omega) + \text{c.c.}]. \quad (4)$$

We now assume that the electron beam interacts with the material, for example, by inducing a plasmon excitation. Let v_{pl} be the velocity component in the direction of the momentum of the excitation. Due to the negative electron charge $-e$, the corresponding component of the current $j_{\text{pl}} = -v_{\text{pl}}e\delta(\mathbf{r} - \mathbf{v}t)$ points in the opposite direction. The electron is here treated as a point charge traveling at the velocity \mathbf{v} . The Fourier transform is $j_{\text{pl}} = -2\pi v_{\text{pl}}e\delta(\omega - k_z v)$. We define $\hbar\mathbf{k}$ to be the momentum gained by the deflected electron. The wave vector \mathbf{k} is antiparallel to the excitation momentum. For the large velocities used in transmission electron microscopes (TEMs), the energy loss is predominantly caused by the change in velocity in the z direction. Then, the Hamilton equation $\partial E / \partial p = v$ and $\Delta p = \hbar k_z$ together with the above delta function reveal that the momentum loss in the z direction is fully determined by the energy loss and the initial electron velocity. We can also Fourier-transform to the $(\mathbf{k}_{\parallel}, z; \omega)$ representation,

which gives

$$j_{\text{pl}}(\mathbf{k}_{\parallel}, z; \omega) = -e \frac{\omega}{v \sqrt{k_{\parallel}^2 + (\omega/v)^2}} e^{i\omega z/v}, \quad (5)$$

where we have used $v_{\text{pl}}/v = k_z/k$ and $k = \sqrt{k_{\parallel}^2 + (\omega/v)^2}$. The electric displacement field \mathbf{D} created by the electron fulfills $\nabla \mathbf{D} = 4\pi e \delta(\mathbf{r} - \mathbf{v}t)$. Fourier transformation in the same way as above for the component in the direction of the plasmon momentum yields the decelerating field

$$E_{\text{pl}}(\mathbf{k}_{\parallel}, z; \omega) = \frac{4\pi e}{i\varepsilon(\mathbf{k}, \omega)} \frac{1}{v \sqrt{k_{\parallel}^2 + (\omega/v)^2}} e^{i\omega z/v}, \quad (6)$$

where we have introduced the dielectric function by $\varepsilon(\mathbf{k}, \omega) \mathbf{E}(\mathbf{k}, \omega) = \mathbf{D}(\mathbf{k}, \omega)$. Combining Eqs. (4)–(6) finally gives the differential scattering cross section as

$$\frac{\partial^3 P}{\partial^2 k_{\parallel} \partial \omega} = -\frac{e^2}{\pi^2 \hbar} \frac{1}{v^2 k^2} \text{Im} \varepsilon^{-1}(\mathbf{k}, \omega) \quad (7)$$

with $k^2 = k_{\parallel}^2 + (\omega/v)^2$.

III. MOMENTUM INTEGRATION

In an EELS experiment, the differential scattering cross section is measured as a function of frequency ω (or energy $\hbar\omega$). If the detector is placed at different angles from normal incidence, one can also record EELS spectra for different in-plane wave vectors \mathbf{k}_{\parallel} . For fixed \mathbf{k}_{\parallel} , there are formally two ω -dependent functions that contribute to the spectrum, the imaginary part of the inverse macroscopic dielectric function $\text{Im} \varepsilon^{-1}(\mathbf{k}, \omega)$ and the prefactor $1/k^2 = 1/[k_{\parallel}^2 + (\omega/v)^2]$. The dielectric function is responsible for the spectral features (peak structure) of the spectrum, whereas the second term merely acts as a weight function, giving low energies a higher weight than higher energies, without altering the overall peak structure. All this explains why $-\text{Im} \varepsilon^{-1}(\mathbf{k}, \omega)$ is commonly regarded as giving the theoretical EELS spectrum.

However, the prefactor $1/k^2 = 1/[k_{\parallel}^2 + (\omega/v)^2]$ does play an important role in the momentum-integrated spectrum, as its \mathbf{k}_{\parallel} dependence governs the relative importance of different \mathbf{k}_{\parallel} vectors. To further assess its role, it is helpful to estimate the orders of magnitude of the different quantities. At an energy loss of 6 eV and an electron velocity of 30% of the speed of light (typically used in a TEM for a thin specimen), the momentum transfer in the z direction is quite small, $k_z = \omega/v = 0.01 \text{ \AA}^{-1}$. Thus, one would expect the prefactor to be approximately ω independent, $1/[k_{\parallel}^2 + (\omega/v)^2] \approx 1/k_{\parallel}^2$, unless the in-plane momentum transfer k_{\parallel} is in the order of magnitude of 0.01 \AA^{-1} or smaller. To a first approximation, one may then be led to neglect ω/v altogether (as it is much smaller than k_{\parallel} nearly everywhere in the Brillouin zone) and retain only $1/k_{\parallel}^2$ when performing the \mathbf{k}_{\parallel} integration. However, since the \mathbf{k}_{\parallel} integration is over a two-dimensional sheet in reciprocal space, the prefactor $1/k_{\parallel}^2$ would always make the integral diverge. As a consequence, we cannot neglect ω/v despite its seeming insignificance, as it makes the integrand around $k_{\parallel} = 0$ and, thus, the integrated values finite.

We want to note that the experimental momentum resolution is typically limited to about 0.1 \AA^{-1} [6], implying that the

experimental spectrum should be understood as a spectrum integrated over a respective range of \mathbf{k}_{\parallel} even in the case of momentum resolution. In the following, we consider the opposite case of an EELS experiment operated in spatial resolution mode, which requires a \mathbf{k}_{\parallel} integration over a complete two-dimensional plane in reciprocal space.

When integrating over momentum transfers \mathbf{k}_{\parallel} ,

$$P'(\omega) = -\frac{e^2}{\pi^2 \hbar v^2} \int \frac{\text{Im}[\varepsilon^{-1}(\mathbf{k}, \omega)]}{k_{\parallel}^2 + (\omega/v)^2} d^2 k_{\parallel}, \quad (8)$$

special care has to be taken for the region around $k_{\parallel} = 0$ for two reasons. First, as we will see later on, the supercell convergence for small (or vanishing) k_{\parallel} is very slow. Second, the loss function [Eq. (7)] varies over several orders of magnitude in this region due to the prefactor, as discussed above. To treat this important region as accurately as possible, we split the integrand into two parts, $P'(\omega) = P'_1(\omega) + P'_2(\omega)$, a (simplified) nearly divergent one,

$$P'_1(\omega) = -\frac{e^2}{\pi^2 \hbar v^2} \int_{k_{\parallel} < k_c} \frac{\text{Im}[\hat{\mathbf{k}}_{\parallel}^T \varepsilon^{-1}(\omega) \hat{\mathbf{k}}_{\parallel}]}{k_{\parallel}^2 + (\omega/v)^2} d^2 k_{\parallel}, \quad (9)$$

which is integrated analytically, and the remainder,

$$P'_2(\omega) = -\frac{e^2 A}{\pi^2 \hbar v^2} \sum_{k_{\parallel} \neq 0} \frac{\text{Im}[\varepsilon^{-1}(\mathbf{k}, \omega)]}{k_{\parallel}^2 + (\omega/v)^2}, \quad (10)$$

which behaves smoothly around $k_{\parallel} = 0$ and which can be integrated efficiently on an equidistant two-dimensional mesh of \mathbf{k} points.

The integration area of Eq. (9) is circular with radius k_c and the center at $\mathbf{k}_{\parallel} = \mathbf{0}$. The radius is chosen such that the disk area equals the area A per mesh point of Eq. (10), so $A = \pi k_c^2$. Furthermore, it has been taken into account in Eq. (9) that the inverse dielectric function at $\mathbf{k} = \mathbf{0}$ is a tensor quantity, here indicated by a boldface ε^{-1} , with two distinguishable entries, in-plane $\varepsilon_{\parallel}^{-1}$ and out-of-plane ε_{\perp}^{-1} . With $\hat{\mathbf{k}}^T \varepsilon^{-1}(\omega) \hat{\mathbf{k}} = [k_{\parallel}^2 \varepsilon_{\parallel}^{-1}(\omega) + (\omega/v)^2 \varepsilon_{\perp}^{-1}(\omega)]/k^2$ and polar coordinates, Eq. (9) can be expressed with the help of two analytic functions

$$P'_1(\omega) = -\frac{e^2}{\pi \hbar v^2} \left\{ \text{Im}[\varepsilon_{\perp}^{-1}(\omega) - \varepsilon_{\parallel}^{-1}(\omega)] f_1\left(\frac{\omega}{vk_c}\right) + \text{Im} \varepsilon_{\parallel}^{-1}(\omega) f_2\left(\frac{\omega}{vk_c}\right) \right\} \quad (11)$$

with

$$f_1(x) = \frac{1}{x^2 + 1}, \quad (12)$$

$$f_2(x) = \ln\left(1 + \frac{1}{x^2}\right). \quad (13)$$

It is important to note that the final expression depends on the full dielectric tensor. The out-of-plane component of the dielectric tensor becomes important for small momentum transfers, small electron velocities, or high energies. Combining this analytic solution with the summation over multiple momentum transfers [Eq. (10)] on an evenly distributed mesh yields the \mathbf{k} -integrated EELS spectrum Eq. (8). Numerical results will be presented in Sec. VIII.

IV. RANDOM-PHASE APPROXIMATION

The dielectric function can be calculated from linear response theory using time-dependent density-functional theory (TDDFT) [19,20]. Neglecting the exchange-correlation kernel of TDDFT corresponds to the random-phase approximation [21,22]. This is the approach that we employ in the present work. It will turn out to be well suited for our purpose. In the random-phase approximation (RPA), the microscopic dielectric function is given by

$$\varepsilon(\mathbf{r}, \mathbf{r}'; \omega) = \delta(\mathbf{r} - \mathbf{r}') - \int v(\mathbf{r} - \mathbf{r}'') P(\mathbf{r}'', \mathbf{r}'; \omega) d^3 r'', \quad (14)$$

with the polarizability

$$P(\mathbf{r}, \mathbf{r}'; \omega) = 2 \sum_n^{\text{occ}} \sum_{n'}^{\text{unocc}} \varphi_n^*(\mathbf{r}) \varphi_n(\mathbf{r}') \varphi_{n'}(\mathbf{r}) \varphi_{n'}^*(\mathbf{r}') \times \left[\frac{1}{\omega + \varepsilon_n - \varepsilon_{n'} + i\eta} - \frac{1}{\omega - \varepsilon_n + \varepsilon_{n'} - i\eta} \right]. \quad (15)$$

Here, $\{\varphi_n(\mathbf{r}), \varepsilon_n\}$ is a complete set of Kohn-Sham eigenfunctions and η is a positive infinitesimal. The Bloch vector is suppressed for simplicity. Furthermore, we assume a non-spin-polarized system, hence the factor 2 instead of an explicit spin summation.

Equation (14) gives the microscopic dielectric function, whereas the dielectric function of Eqs. (6) and (7) is the macroscopic one. In a plane-wave representation, the latter can be obtained from the former by [21,23]

$$\varepsilon(\mathbf{k}, \omega) = \frac{1}{\varepsilon_{00}^{-1}(\mathbf{k}, \omega)}, \quad (16)$$

where

$$\varepsilon_{\mathbf{G}\mathbf{G}'}(\mathbf{k}, \omega) = \frac{1}{V} \iint e^{-i(\mathbf{k}+\mathbf{G})\mathbf{r}} \varepsilon(\mathbf{r}, \mathbf{r}'; \omega) e^{i(\mathbf{k}+\mathbf{G}')\mathbf{r}'} d^3 r d^3 r' \quad (17)$$

is the plane-wave representation of the microscopic function. The prefactor $1/V$ originates from the normalization of the plane waves $e^{i(\mathbf{k}+\mathbf{G})\mathbf{r}}/\sqrt{V}$ with the supercell volume V . We note that we do not employ a plane-wave representation in our computational approach but a representation in the mixed product basis [24]. However, apart from a trivial difference in basis indices, the formulas are analogous to the plane-wave case. For simplicity, we therefore adopt a plane-wave formulation here and in the following.

For periodic systems, the polarizability of Eq. (15) can be written as a Fourier transform $P_{\mathbf{G}\mathbf{G}'}(\mathbf{k}, \omega)$. Its head element $P_{00}(\mathbf{k}, \omega)$ can be shown to be proportional to k^2 for $\mathbf{k} \sim \mathbf{0}$. This factor cancels when multiplying with $v(\mathbf{k}) = 4\pi/k^2$ in (the Fourier-transformed) Eq. (14). In addition, the polarizability exhibits an angular dependence around $\mathbf{k} = \mathbf{0}$ in reciprocal space; i.e., $\lim_{\mathbf{k} \rightarrow \mathbf{0}} P_{00}(\mathbf{k}, \omega)/k^2$ depends on the direction $\hat{\mathbf{k}}$ from which $\mathbf{k} = \mathbf{0}$ is approached. This angular dependence transfers to the dielectric function, which, at $\mathbf{k} = \mathbf{0}$, can be formulated in vector form by $\varepsilon(\mathbf{k}, \omega) \sim \hat{\mathbf{k}}^T \boldsymbol{\varepsilon}(\omega) \hat{\mathbf{k}}$. In the present 2D systems, the 3×3 dielectric tensor has

the form

$$\boldsymbol{\varepsilon}(\omega) = \begin{pmatrix} \varepsilon_{\parallel}(\omega) & 0 & 0 \\ 0 & \varepsilon_{\parallel}(\omega) & 0 \\ 0 & 0 & \varepsilon_{\perp}(\omega) \end{pmatrix}. \quad (18)$$

The structural anisotropy of the 2D systems is thus reflected in their dielectric properties. The “inverse” tensor $\boldsymbol{\varepsilon}^{-1}(\omega)$ used in Sec. III is to be understood as the tensor approximating $\hat{\mathbf{k}}^T \boldsymbol{\varepsilon}^{-1}(\omega) \hat{\mathbf{k}} \approx 1/[\hat{\mathbf{k}}^T \boldsymbol{\varepsilon}(\omega) \hat{\mathbf{k}}]$, which, in an anisotropic system, does not simplify to $\boldsymbol{\varepsilon}^{-1}(\omega) = [\boldsymbol{\varepsilon}(\omega)]^{-1}$ [24]. Here, “approximating” means that the left-hand side is identical to the right-hand side up to second order in the components of $\hat{\mathbf{k}}$.

To explain that in more detail, consider both sides to be expressed exactly in terms of spherical harmonics,

$$\sum_{l=0}^{\infty} \sum_{m=-l}^l \varepsilon_{lm}^{-1}(\omega) Y_{lm}(\hat{\mathbf{k}}) = \left[\sum_{l'=0}^2 \sum_{m'=-l'}^{l'} \varepsilon_{l'm'}(\omega) Y_{l'm'}(\hat{\mathbf{k}}) \right]^{-1}, \quad (19)$$

with suitable coefficients $\varepsilon_{lm}^{-1}(\omega)$ and $\varepsilon_{l'm'}(\omega)$. The latter coefficients are known; the former are unknown. Multiplying with the expression in the square brackets, using $Y_{lm}(\hat{\mathbf{k}}) Y_{l'm'}(\hat{\mathbf{k}}) = \sum_{l'', m''} G_{lm, l'm', l'' m''} Y_{l'' m''}(\hat{\mathbf{k}})$ with the Gaunt coefficients $G_{lm, l'm', l'' m''} = \int Y_{lm}(\Omega) Y_{l'm'}(\Omega) Y_{l'' m''}^*(\Omega) d\Omega$, and equating the resulting coefficients yields a system of linear equations, which can be solved for the unknown coefficients $\varepsilon_{lm}^{-1}(\omega)$, of which only the coefficients for $l \leq 2$ are relevant for the approximation. In practice, the l summation in Eq. (19) must be truncated, and its upper bound becomes a convergence parameter.

V. SUPERCELL CONVERGENCE

The SPEX code [24] employs periodic boundary conditions in all three spatial directions. While the 2D translational periodicity of an infinite monolayer is thus fully incorporated, the periodicity in the third direction leads to a periodic stacking of layers. The interlayer distance, governed by the size of the supercell perpendicular to the layers, becomes a convergence parameter: Results have to be converged with respect to larger and larger interlayer spacings minimizing the coupling between the monolayers.

In the present case, the convergence can be particularly slow because dielectric screening is mediated by the Coulomb interaction and is, thus, a long-range phenomenon. So, even though the electron density falls off exponentially into the vacuum and the orbitals of neighboring layers do not overlap, the slow convergence due to the interlayer screening causes a major bottleneck for EELS calculations.

Let us first make a few general observations about the supercell convergence for the monolayer. Since the atom-thick or few-atoms-thick monolayer keeps its thickness, the average material density decreases as we increase the supercell size in the z direction, and the macroscopic quantities will approach more and more their vacuum values: 1 for the dielectric function and 0 for the polarizability. The polarizability is the independent-particle density response function giving the linear change of the electronic density with respect to changes in the effective potential. Clearly, the less electron density there is on average, the smaller its average response.

In the supercell limit, it reduces to zero. As a consequence, the macroscopic inverse dielectric function becomes 1 and its imaginary part zero. This leads to a curious situation in which the supercell size needs to be converged to eliminate interlayer interactions, but, in doing so, the EELS signal disappears [see Eq. (7)]. A way of resolving this issue is to remember that the supercell limit is somewhat unphysical in its own right. It would presuppose an infinite laboratory or, equivalently, a sample of vanishing thickness. (No wonder then that the signal disappears.) The sample is atomically thin, but it does have a finite size, thick enough to be measured. To make the supercell convergence meaningful, one should thus scale the theoretical spectrum by the supercell size, e.g., by its height L . Also note that this scaling eliminates the normalization factor $1/V$ (up to prefactors) in the matrix representation of P [analogous to Eq. (17)]. The normalization factor is responsible for the vanishing spectrum. In fact, spectra scaled in this way do converge. Of course, this issue is nothing new and has already been discussed before. Another way of looking at it is to remember that, as we increase the supercell size, the momentum grid gets denser and denser. It is then clear that, when, in the supercell limit, the momenta lie infinitely close to each other, an experiment cannot pick out a particular crystal momentum out of a continuity of uncountably many momenta but would include all momenta within a small but finite region in reciprocal space around a given crystal momentum. The density of the momenta scales with the supercell volume V (or height L), thus canceling the factor $1/V$.

If one assumes the scaled head of the polarization matrix $p(\mathbf{k}, \omega) = L \cdot P_{00}(\mathbf{k}, \omega)$ to be approximately independent of the interlayer distance (which is a good approximation), then taking the supercell limit of the scaled imaginary part of the inverse macroscopic dielectric function yields (in simplified notation)

$$\begin{aligned} -\lim_{L \rightarrow \infty} L \cdot \text{Im} \varepsilon^{-1} &= -\lim_{L \rightarrow \infty} \text{Im} \frac{L}{1 - vP} \\ &= -\lim_{L \rightarrow \infty} \frac{v \text{Im} p}{[\text{Re}(1 - vP/L)]^2 + [\text{Im}(vP/L)]^2} \\ &= -v \text{Im} p = \lim_{L \rightarrow \infty} L \cdot \text{Im} \varepsilon, \end{aligned} \quad (20)$$

giving the interesting result that the EELS spectrum ($-\text{Im} \varepsilon^{-1}$) of 2D systems equals the absorption spectrum ($\text{Im} \varepsilon$) in the supercell limit [25]. We can thus use either of the two expressions. For example, we may choose the one that converges fastest.

The speed of convergence of $-\text{Im} \varepsilon^{-1}(\mathbf{k}, \omega)$ with respect to the supercell size depends on the lateral component of the Bloch vector \mathbf{k}_{\parallel} . The inverse dielectric function converges much faster for large \mathbf{k}_{\parallel} than for small or vanishing \mathbf{k}_{\parallel} . This qualitative behavior is easily understood. The component \mathbf{k}_{\parallel} in $\varepsilon^{-1}(\mathbf{k}, \omega)$ gives the periodicity of the induced charge density and thus of the screening field within the layers. In the case of large \mathbf{k}_{\parallel} and correspondingly short wavelengths, the induced electron density in the layer quickly oscillates between + and - charges so that the induced potential falls off quickly into the vacuum. The neighboring layers will hardly “feel” this potential, and this effective decoupling of the interlayer screening enables a fast supercell convergence.

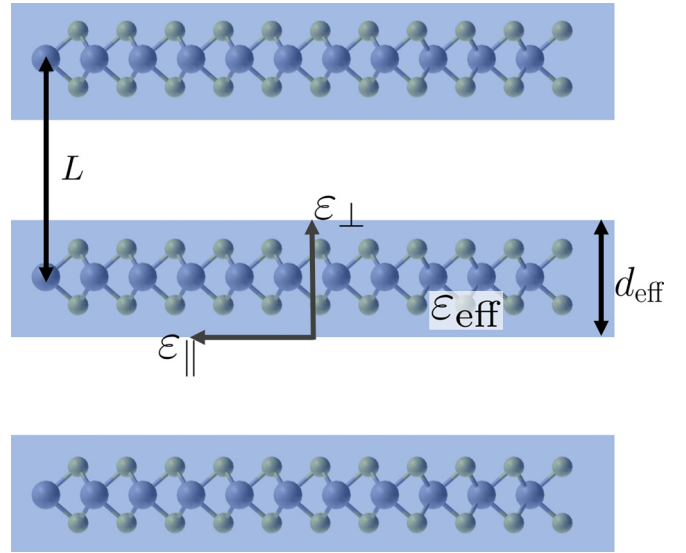


FIG. 1. Illustration of a monolayer with periodic images for a supercell of height L with the components of the dielectric tensor ε_{\parallel} and ε_{\perp} as well as the model parameters ε_{eff} and d_{eff} .

Conversely, for small wave vectors, the convergence of $-\text{Im} \varepsilon^{-1}(\mathbf{k}, \omega)$ can be very slow. As we have seen in Sec. II, the low- \mathbf{k} contributions get a weight of $1/k^2$ and are therefore particularly important for the \mathbf{k}_{\parallel} -integrated EELS spectrum. We have to make sure that all contributions $\varepsilon^{-1}(\mathbf{k}, \omega)$ are sufficiently converged before performing the \mathbf{k}_{\parallel} integrations and summations of Eqs. (10) and (11).

Let us now have a closer look at the limit $\mathbf{k} \rightarrow \mathbf{0}$. It is instructive to investigate this limit with the help of a model of repeated homogeneous dielectric slabs as illustrated in Fig. 1. The model has only three parameters: the layer distance L (measured from center to center), the effective layer thickness d_{eff} , and the effective dielectric constant ε_{eff} of the slabs. The atomistic layer structure is superimposed on the slabs in Fig. 1 only for illustrative purposes. The parameter L corresponds to the supercell height and is thus not a free parameter. At first, it seems that the parameter d_{eff} cannot be clearly determined from the atomistic model used in the *ab initio* calculations, since the electron density falls off exponentially on either side of the layer. So, there is no abrupt drop of the electron density, which would be required for a unique definition of d_{eff} . The same holds for ε_{eff} .

However, we can determine these model parameters from the following two equations based on effective medium theory [26]:

$$\varepsilon_{\perp}^{-1} = \frac{d_{\text{eff}}}{L} \varepsilon_{\text{eff}}^{-1} + \frac{L - d_{\text{eff}}}{L}, \quad (21)$$

$$\varepsilon_{\parallel} = \frac{d_{\text{eff}}}{L} \varepsilon_{\text{eff}} + \frac{L - d_{\text{eff}}}{L}, \quad (22)$$

with the two components of the dielectric tensor ε_{\parallel} and ε_{\perp} calculated from first principles (see Sec. IV). The equations can be motivated from basic summation rules of capacitances. In the perpendicular direction, the layers act as capacitors connected in series. The total capacitance in this case is the reciprocal value of the sum of reciprocal values of all

capacitances. Likewise, the second equation corresponds to capacitors connected in parallel, in which case the total capacitance is simply the sum of all capacitances. Expressing the capacitances with the model parameters leads to Eqs. (21) and (22).

The parameters d_{eff} and ε_{eff} determined from Eqs. (21) and (22) turn out to be approximately independent of the layer distance L and can thus be regarded as material parameters. In the case of a multilayer slab, one can still define d_{eff} and ε_{eff} , which then reflect the combined effect of all layers. Equation (20) has taught us that $-L \cdot \text{Im } \varepsilon_{\parallel}^{-1}$ and $L \cdot \text{Im } \varepsilon_{\parallel}$ converge to the same limit. We can now check which series converges faster for the present case of $\mathbf{k} \rightarrow \mathbf{0}$. Using Eq. (22), it is straightforward to show that it is the latter series: $\lim_{L \rightarrow \infty} L \cdot \text{Im } \varepsilon_{\parallel} = d_{\text{eff}} \text{Im } \varepsilon_{\text{eff}}$. So, for large \mathbf{k}_{\parallel} , $-L \text{Im } \varepsilon_{\parallel}^{-1}$ converges faster, whereas for vanishing \mathbf{k}_{\parallel} , $L \text{Im } \varepsilon_{\parallel}$ converges faster. (Interestingly, the opposite is true for ε_{\perp} .) Clearly, for \mathbf{k}_{\parallel} vectors in between, neither of the two series will converge quickly. In this general case, we can make use of an extrapolation formula, which will be discussed in the next section and which does not rely on any model parameters.

VI. SUPERCCELL EXTRAPOLATION FORMULA

Since the supercell convergence can become very costly, in particular for intermediate \mathbf{k}_{\parallel} , we employ here an extrapolation formula, which was derived in Ref. [17]; see our Appendix here. The extrapolation formula aims at extrapolating from the repeated slab system (Fig. 1) to the monolayer including the effects of momentum transfer. This will allow for a very fast convergence with respect to the interlayer distance in the repeated slab system and therefore enable us to use a minimal amount of vacuum in between the layers and so reduce the computational effort.

We quote the supercell extrapolation formula of Ref. [17] and then show that it reproduces the series in the two special limits discussed in the previous section. For completeness, a derivation is sketched in the Appendix. The formula gives the L -scaled imaginary part of the inverse macroscopic dielectric function extrapolated to the supercell limit $L \rightarrow \infty$,

$$-\lim_{L \rightarrow \infty} L \text{Im } \varepsilon^{-1}(\mathbf{k}_{\parallel}, \omega; L) \approx -\text{Im} \frac{L}{\frac{1}{\varepsilon_{00}^{-1}(\mathbf{k}_{\parallel}, \omega; L) - 1} + \frac{k_{\parallel} L}{e^{k_{\parallel} L} - 1}}, \quad (23)$$

where we have explicitly included L as an argument in $\varepsilon^{-1}(\mathbf{k}_{\parallel}, \omega; L)$, the inverse macroscopic dielectric function calculated in a supercell with height L . It is important to understand that the limit $L \rightarrow \infty$ is only taken on the left-hand side, whereas the right-hand expression is determined from results of a supercell calculation with finite L . So, for each L , we get a different extrapolated macroscopic dielectric function. The corresponding series for larger and larger L converges rapidly for each \mathbf{k}_{\parallel} , as will be shown in the following.

Let us first consider the two cases $k_{\parallel} \rightarrow 0$ and $k_{\parallel} \rightarrow \infty$. In the latter, the second term in the denominator of the right-hand side vanishes. Due to the exponential function, this term becomes negligible already for intermediate to large k_{\parallel} . One thus obtains the series $-L \text{Im } \varepsilon^{-1}(\mathbf{k}_{\parallel}, \omega; L)$ on the right-hand

side. In the limit $k_{\parallel} \rightarrow 0$, the second term in the denominator becomes unity, yielding the series $L \text{Im } \varepsilon(\mathbf{k}_{\parallel}, \omega; L)$. So, the extrapolation formula in Eq. (23) indeed reproduces the two series we identified in Sec. V as the fastest convergent ones in the two limiting cases.

The extrapolation formula generally yields rapidly convergent series for all \mathbf{k}_{\parallel} . Figure 2 shows, from left to right, the loss spectrum $-\text{Im } \varepsilon^{-1}(\mathbf{k}_{\parallel}, \omega; L)$, the absorption spectrum $\text{Im } \varepsilon(\mathbf{k}_{\parallel}, \omega; L)$, and the extrapolated spectrum according to Eq. (23) for the four wave vectors $k = 0$, $k = 0.04 \text{ \AA}^{-1}$, $k = 0.12 \text{ \AA}^{-1}$, and $k = 0.20 \text{ \AA}^{-1}$ from top to bottom. The spectra were calculated with supercells of different heights from 12.3 Å to 123 Å; see legend inset. The top left and bottom middle panels demonstrate the fast convergence for the two special cases discussed in the previous section. The extrapolated spectra presented in the right column exhibit consistently fast convergence for all wave vectors. In fact, in each panel on the right, there are six curves for the six different supercell heights L , but they are all nearly identical and practically lie on top of each other.

VII. COMPUTATIONAL DETAILS

In Sec. VIII, we present the \mathbf{k}_{\parallel} -integrated EELS spectra Eq. (8) as obtained from Eqs. (10) and (11). It turns out that the terms in Eq. (10) fall off rapidly with \mathbf{k}_{\parallel} (note the factor $1/k^2$), which allows us to neglect contributions of large \mathbf{k}_{\parallel} . For the present materials, it is found that momentum transfers only within the first 2D Brillouin zone need to be considered (or even fewer). We employ an evenly distributed mesh across the 2D Brillouin zone for the \mathbf{k}_{\parallel} summation of Eq. (10), taking advantage of the crystal symmetries by further restricting the \mathbf{k}_{\parallel} points to the irreducible wedge of the 2D Brillouin zone.

There are two parameters in Eq. (10) that are not fundamental physical or mathematical constants. First, A is the reciprocal area per \mathbf{k}_{\parallel} point (total area covered by the mesh divided by the number of mesh points). Second, v is the speed of the incoming electrons. Here, we use $v = 80 \text{ keV}$ for all materials, which is a typical speed used in TEM experiments on monolayer systems. The parameter A also appears implicitly in the relation $A = \pi k_c^2$ for the reciprocal cutoff radius k_c of Eq. (11).

For reasons discussed in Sec. V, Eq. (8) would vanish in the supercell limit ($L \rightarrow \infty$) unless scaled with the layer distance L . We therefore include the factor L and make use of Eq. (23) to extrapolate Eq. (10) to infinite layer distances. For the dielectric tensor components in Eq. (11), the fastest converging series are the absorption spectrum $L \text{Im } \varepsilon_{\parallel}(\omega; L)$ for the parallel component, corresponding to the long-wavelength limit of Eq. (23), and (unaltered) $-L \text{Im } \varepsilon_{\perp}^{-1}(\omega; L)$ for the component perpendicular to the layers. The tensor components and the macroscopic inverse dielectric function $\varepsilon^{-1}(\mathbf{k}_{\parallel}, \omega; L)$ needed for Eq. (23) are evaluated using the RPA [Eq. (15)] combined with the inversion of the microscopic dielectric matrix $\varepsilon_{\mathbf{G}\mathbf{G}'}(\mathbf{k}, \omega; L)$ in order to include local-field effects.

The prefactor of Eq. (8) would merely scale the spectra by a constant $e^2/(\pi^2 \hbar v^2)$ and is therefore neglected. Together with the scaling factor L , the spectra have thus the formal unit of length.

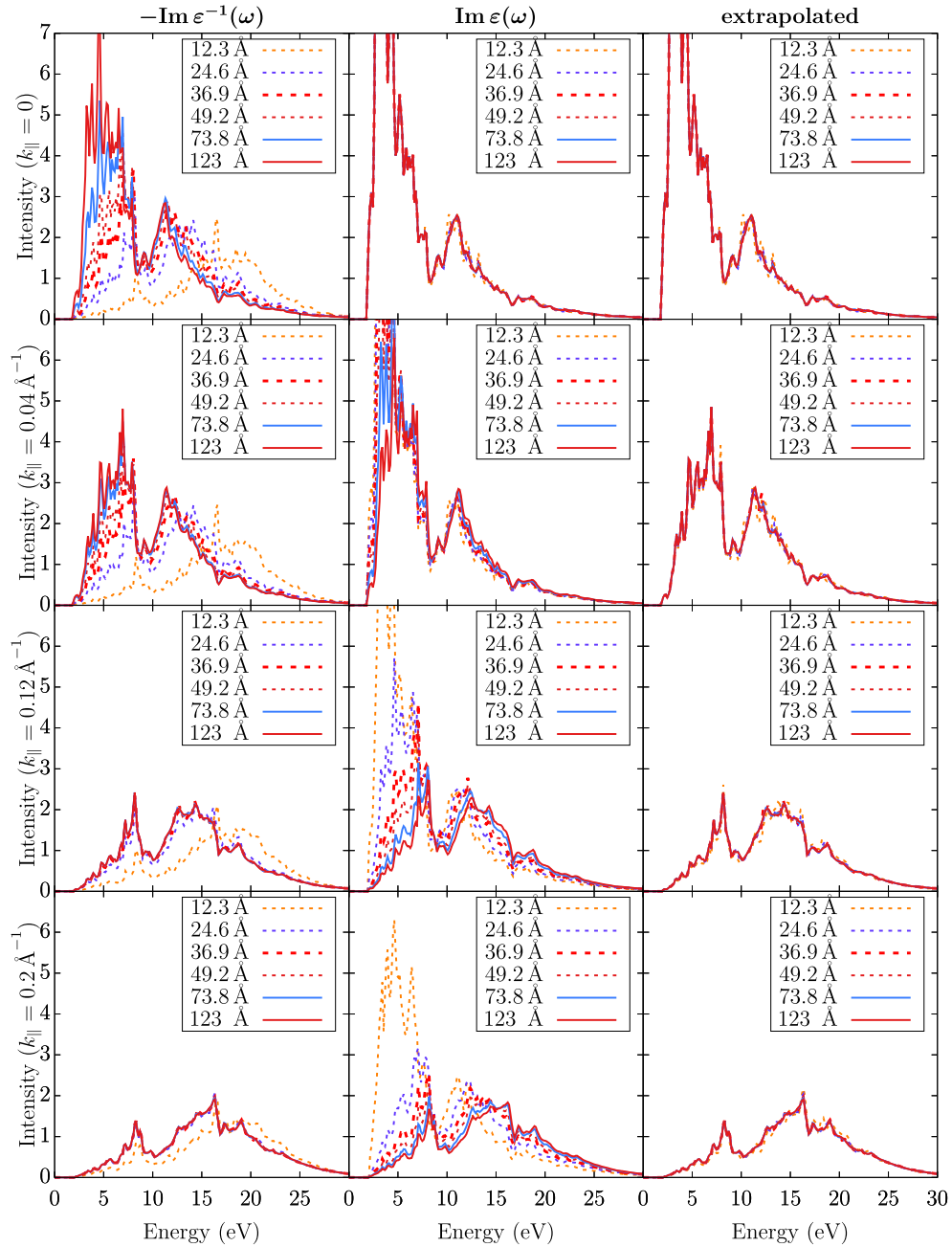


FIG. 2. Scaled EEL spectra ($-L \text{Im} \epsilon^{-1}$, left column), absorption spectra ($L \text{Im} \epsilon$, middle column), and extrapolated spectra [Eq. (23), right column] for several momentum transfers k_{\parallel} and layer distances (supercell heights) L from supercell calculations of a MoS₂ monolayer. The extrapolated spectra exhibit a very fast convergence with respect to L for all k_{\parallel} .

The Kohn-Sham eigensolutions of Eq. (15) are calculated with FLEUR [27], an implementation of density-functional theory (DFT) based on the full-potential linearized augmented-plane-wave (FLAPW) method. We employ the exchange-correlation energy functional in the parametrization of Perdew and coworkers [28] (PBE). The RPA polarizability [Eq. (15)] is subsequently constructed with SPEX [24], an all-electron GW code that employs the same LAPW basis set and a mixed product basis to represent two-particle quantities such as the polarizability $P(\mathbf{r}, \mathbf{r}'; \omega)$ and the microscopic dielectric function $\epsilon(\mathbf{r}, \mathbf{r}'; \omega)$ [Eq. (14)]. The microscopic and

macroscopic dielectric functions are related according to Eqs. (16) and (17).

The scheme is applied to three monolayer systems, semiconducting MoS₂, insulating hBN, and semimetallic graphene. We employ the experimental lattice constants of the layered bulk systems, $a = 3.15 \text{ \AA}$ [29], $a = 2.504 \text{ \AA}$ [30], and $a = 2.462 \text{ \AA}$ [31], for MoS₂, hBN, and graphene, respectively. The boron nitride and graphene monolayers are atomically thin, while the molybdenum disulfide monolayer consists of a Mo layer sandwiched between two S layers. Here, we adopt the bulk structure but allow for a relaxation of the sulfur

layers in the perpendicular direction up to a residual force of 5×10^{-2} eV/Å. The relaxed positions of the sulfur layers are at $c(1/4 - z)$ and $c(z - 1/4)$ relative to the Mo layer with the bulk lattice constant $c = 12.3$ Å and the internal coordinate $z = 0.124$, in very good agreement with the experimental and theoretically optimized structure of the bulk phase [32].

The DFT calculations are carried out on grids of $10 \times 10 \times 1$ ($14 \times 14 \times 1$) \mathbf{k} points for MoS₂ (hBN and graphene) monolayers. The LAPW plane-wave cutoff is set to 4.1 a.u. (4.5 a.u.). The maximal muffin-tin l -quantum number is ten for molybdenum and eight for sulfur. For the second-row elements boron, carbon, and nitrogen, we have consistently used a maximal l -quantum number of six. To treat the semicore $4s$ and $4p$ states, we employ local orbitals with the respective orbital characters in the molybdenum muffin-tin spheres.

The polarizability [Eq. (15)] involves a summation over occupied and unoccupied states as well as over \mathbf{k} points. Here, we have employed a grid of $12 \times 12 \times 1$ ($42 \times 42 \times 1$) \mathbf{k} points for MoS₂ (hBN and graphene) monolayers and the tetrahedron method [33] to interpolate between the \mathbf{k} points. The band summations comprise 190 bands for all materials. A fine frequency (ω) mesh between 0 and 2 hartree has been employed with an increment of 0.005 hartree and a total number of 401 frequency mesh points. We show a smaller range (0 to 30 eV) in the diagrams.

For the summation in Eq. (10), we find that the \mathbf{k}_{\parallel} -point set should have the point density of an equidistant 100×100 grid of the 2D Brillouin zone, but, as the integrand falls off quickly with k_{\parallel} , we do not always need to include all 100×100 points. For example, for hBN and graphene, we can truncate the set to 20×20 while leaving the \mathbf{k} -point density unchanged. In addition, spatial and time-reversal symmetry is exploited to reduce the number of \mathbf{k} points.

The Kohn-Sham DFT band gap is adjusted with a scissor operator to align with the experimental band gap (onset of EEL spectra) to address the well-known underestimation of the band gap of Kohn-Sham DFT.

VIII. RESULTS

Figure 3 illustrates the impact of the extrapolation formula [Eq. (23)] on the \mathbf{k}_{\parallel} -integrated EEL spectrum for the MoS₂ monolayer. The red and blue curves show the respective spectra with and without making use of the extrapolation formula. The spectra differ substantially below 8 eV, where the blue spectrum (without extrapolation) is missing a lot of intensity. Note that the blue curve corresponds to summing the spectra in the first column of Fig. 2, which show a particularly bad supercell convergence for small momentum transfers. Due to the factor $1/k^2$, it is precisely the small momentum transfers that play an important role for the \mathbf{k}_{\parallel} -integrated spectrum. Their slow supercell convergence has thus a detrimental effect on the results. Comparing the missing intensity with the absorption spectrum (orange line), which corresponds to the extrapolated EEL spectrum for $\mathbf{k} = \mathbf{0}$, corroborates that the underconverged partial spectra are responsible for the missing intensity in the blue curve.

As an alternative to the extrapolation formula, one can, of course, employ very large supercells. This solves the

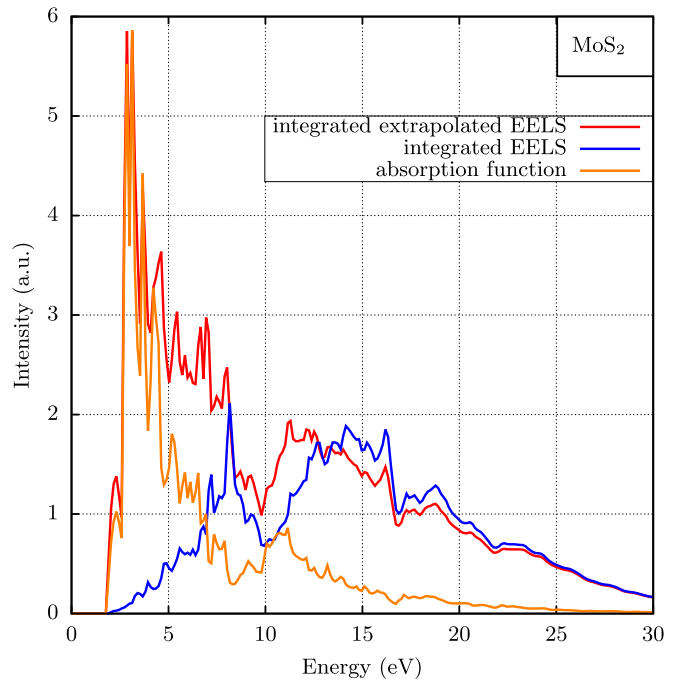


FIG. 3. \mathbf{k}_{\parallel} -integrated EELS for a MoS₂ monolayer with and without extrapolation (red and blue lines). The absorption spectrum $\text{Im } \epsilon_{\parallel}(\omega)$ ($\mathbf{k} = \mathbf{0}$) is shown as well (orange line). For all calculations a layer distance (supercell height) of 24.6 Å is used.

forementioned problem, too, but at the price of a high computational cost. Figure 4 presents two theoretical EEL spectra: the red one is calculated with the extrapolation formula, the dashed blue one without but with an enlarged supercell height of 123 Å (up to a momentum transfer of 0.23 \AA^{-1} and 36.9 \AA elsewhere). Both curves are practically on top of each other, thus highlighting the advantage of the extrapolation scheme due to the significantly smaller computational cost.

Figure 4 also contains the experimental EEL spectrum as a black dashed line. It agrees very favorably with the theoretical spectra, in particular when compared to the absorption spectrum of Fig. 3, which lacks a lot of intensity for energies above 5 eV. This intensity thus stems from the contributions of larger momentum transfers, showing the importance of the \mathbf{k}_{\parallel} integration. We note that excitonic effects, which predominantly affect the peak structure at the low-energy onset of the spectra, are neglected in the RPA. Due to the large energy range, modifications due to excitonic contribution would hardly be noticeable, however. Figure 5 presents the theoretical and experimental EEL spectra for a hexagonal boron nitride monolayer. The calculations are done for a layer distance of 50.35 Å (4 bulk unit cells). The boron nitride monolayer is insulating with a large experimental band gap of about 6.1 eV [36]. Kohn-Sham DFT with PBE for the exchange-correlation functional underestimates the band gap and yields 4.67 eV. As before, the theoretical spectrum has been aligned with the experimental spectrum to account for this band-gap underestimation.

Similar to the case of MoS₂, the absorption spectrum of hBN (Fig. 5, orange curve) lacks intensity in the broad peak between 12 and 25 eV in comparison to the experimental

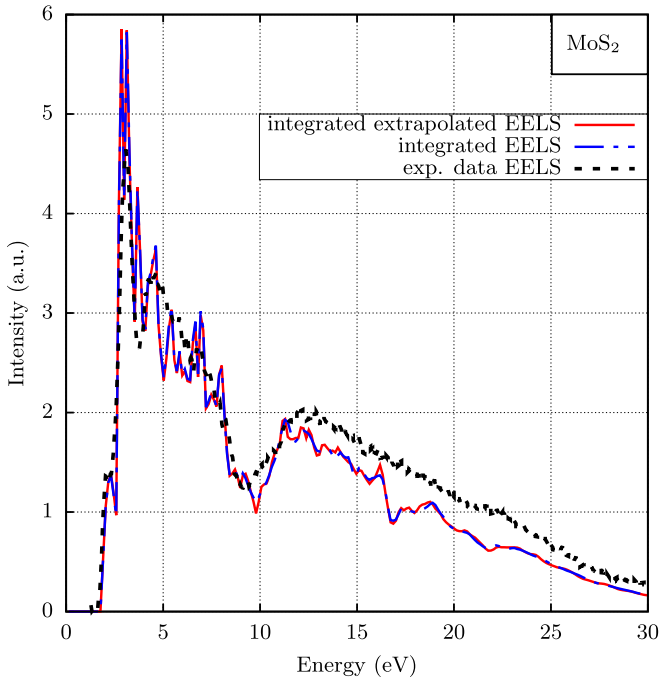


FIG. 4. Comparison of \mathbf{k}_{\parallel} -integrated EEL spectra for MoS₂ using a layer distance of 123 Å (blue) as well as using a distance of 24.6 Å and the extrapolation formula (red). An excellent agreement between the two theoretical curves (the latter at a considerably lower computational cost) and a very good agreement to the experimental spectrum is observed. Experimental EELS data [34] are shown in black. Reproduced by kind permission of John Wiley and Sons.

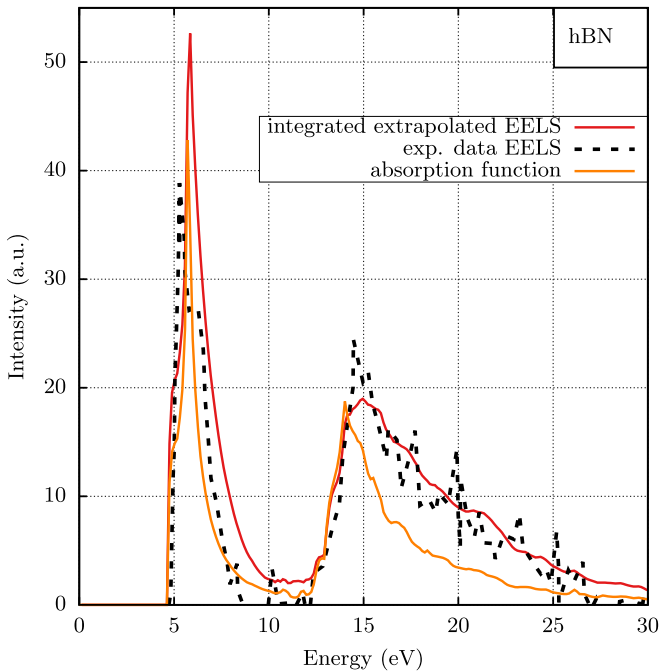


FIG. 5. Comparison of theoretical (red line) and experimental EEL spectra (black dashed line) for monolayer hBN [35]. The absorption spectrum $\text{Im}\epsilon_{\parallel}(\omega)$ ($\mathbf{k} = \mathbf{0}$) is shown in addition (orange line).

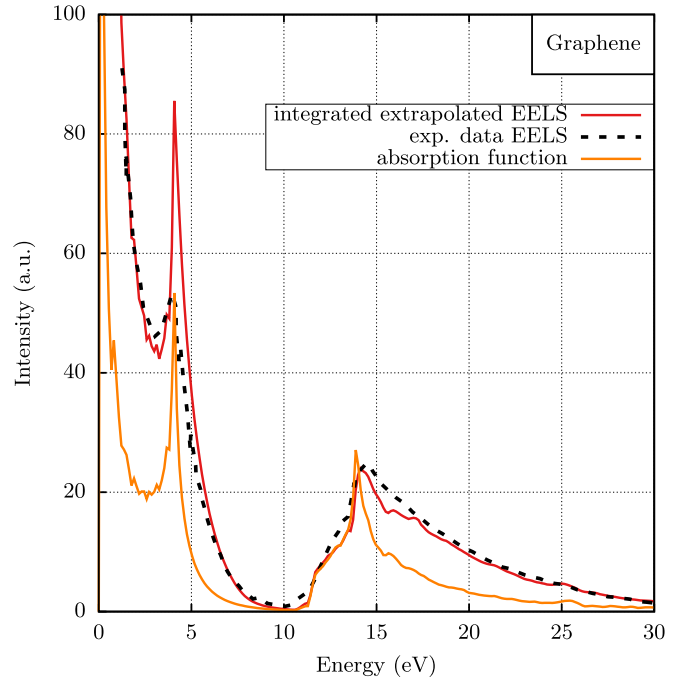


FIG. 6. Same as Fig. 5 for graphene [37]. Reproduced by kind permission of Elsevier.

spectrum, in particular for higher energies so that the peak appears blueshifted. This is also observed in graphene.

The red line shows the \mathbf{k}_{\parallel} -integrated spectrum. It is evident that the \mathbf{k}_{\parallel} integration makes up the missing intensity so that the resulting spectrum ends up very close to experiment. Closer inspection shows that the intense peak at the low-energy onset (between 5 and 8 eV) exhibits a somewhat different shape in the theoretical spectrum compared to the experimental one. This is likely caused by the neglect of excitonic effects in the theory, which should predominantly affect the low-energy part of the spectrum. Due to the large band gap and the low screening, excitons in hexagonal boron nitride monolayers have a large binding energy.

Finally, after two monolayer systems with an energy gap, we present results for a monolayer of semimetallic graphene in Fig. 6. The graphene monolayer is placed in a supercell with a height of 50.95 Å. The EEL spectrum calculated without \mathbf{k}_{\parallel} integration (orange line), which, in the monolayer limit, corresponds to the absorption spectrum (see Sec. V), lacks intensity on the high-energy side of the broad peak around 15 eV. Similar to MoS₂ and hBN, this missing intensity originates from the contribution of energy losses having finite momentum transfers. These losses are all taken into account (up to 0.5752 \AA^{-1}) with their proper weight in the \mathbf{k}_{\parallel} -integrated spectrum, which is shown as the red solid line. In fact, very good agreement between theory and experiment is achieved. Notably, also the low-energy structure of the EEL spectrum is improved. The metallic divergence of the spectrum for $\omega \rightarrow 0$ is faithfully reproduced, not only qualitatively but also quantitatively. The theoretical curve traces the experimental one quite accurately nearly for the whole displayed energy range, except that the sharp peak at around 4.5 eV seen in the theoretical spectrum is smaller and broader in the

experimental one, possibly caused by the limited energy resolution of the experiment, finite temperature, or defects in the sample material.

IX. CONCLUSIONS

In this work, we have developed a technique to calculate accurate EEL spectra from first principles using the RPA for the polarizability. In particular, we have considered the limit of low momentum resolution, in which case energy losses of a large range of lateral momentum transfers are collected in the experiment. In this sense, the technique is of particular relevance for the measurement of spatially resolved EELS. It has been applied to three monolayer systems, MoS₂, hBN, and graphene.

We have shown that it is possible to achieve very good agreement between experimental loss spectra, measured in a TEM, and the theoretical prediction if the partial spectra are integrated over the lateral momentum transfer \mathbf{k}_{\parallel} taking into account the proper weights from the formula of the theoretical differential scattering cross section. The \mathbf{k}_{\parallel} integration is over all relevant momentum transfers (collected in the aperture of the experimental setup). In the present work, we consider all momenta up to a cutoff, at which the contribution becomes negligible.

The \mathbf{k}_{\parallel} integration is divided into two terms. The first accounts for the important region around $\mathbf{k}_{\parallel} = \mathbf{0}$, where the integrand exhibits very large variations and can become nearly divergent. Fortunately, the respective \mathbf{k}_{\parallel} integral can be carried out analytically. The second term contains the contributions from all other, finite momentum transfers ($|\mathbf{k}_{\parallel}| > 0$), which exhibit a smooth behavior and can thus be summed numerically. Interestingly, the speed of the incoming electrons in the electron beam enters as a parameter, affecting the shape of the resulting EEL spectra.

The calculations are carried out with periodic boundary conditions, which requires the usage of supercells to treat the monolayer systems. The supercells have to be large perpendicular to the layers to eliminate the unwanted layer-layer interactions. It turns out that the calculations are particularly complicated by the fact that very large supercell (or vacuum) sizes are required for the EEL contributions coming from small \mathbf{k}_{\parallel} , making the calculations computationally very demanding.

We were able to reduce the computational effort drastically by making use of an extrapolation formula, which yields an EEL spectrum (for a given \mathbf{k}_{\parallel}) extrapolated to infinite layer distances from the corresponding spectrum calculated with a finite layer distance. A very fast supercell convergence of the extrapolated spectra is observed. With the help of the extrapolation, we could keep the supercells very small, e.g., to a modest 25.6 Å distance of periodic replicas in the case of the MoS₂ monolayer, without compromising accuracy.

We have shown illustrative results for monolayers of MoS₂ (small band gap), hBN (large band gap), and graphene (no band gap) and compared them to experimental EEL spectra. We find very good agreement in all cases. The \mathbf{k}_{\parallel} -integrated spectra are significantly closer to experiment than the EEL spectra calculated for $\mathbf{k} = \mathbf{0}$. The largest difference between theory and experiment is found in the shape of the low-energy

peak in hBN. This difference is probably due to the neglect of excitonic effects in RPA.

The extrapolation formula may allow monolayer systems with large 2D unit cells to be treated, enabling the calculation of more complex systems, for example, multilayer systems and systems with defects. Such systems are currently of particular interest, as the combination of several layers or the introduction of defects can serve as an important tool to tailor electric and optical properties of 2D materials.

ACKNOWLEDGMENTS

We acknowledge the insightful discussions during our regular meetings with Ursel Bangert, Eoin Moynihan, Michael Hennessy, Beata Kardynal, and Minh Bui. This work was partly funded by the project “New single photon sources by engineering monolayer-thick semiconductors on the atomic scale” (Az. 93 427) supported by the “Integration of Molecular Components in Functional Macroscopic System” initiative of the Volkswagen-Stiftung. We acknowledge the computing time granted through JARA-HPC on the supercomputer JURECA at Forschungszentrum Jülich.

APPENDIX: DERIVATION OF EXTRAPOLATION FORMULA

The supercell extrapolation formula used in the present work is very similar to an expression derived by Nazarov *et al.* [17,38] for the 2D dielectric function. In our case, however, we need an extrapolation formula for the 3D dielectric function. Therefore, and for the sake of completeness, we present here an alternative, slightly different derivation.

Let $n_{\mathbf{G}}(z, \mathbf{k}_{\parallel}, \omega)$ be the change of density in the repeated-slabs system induced by an external perturbation. We use a dual representation in 2D Fourier space ($\mathbf{k}_{\parallel}, \mathbf{G}$) for the xy plane (along the layers) and the real-space z coordinate (perpendicular to the layers). We restrict the external perturbation to only vary along the xy plane but not along the z coordinate. The induced potential

$$U_{\mathbf{G}}^{\text{ind}}(z, \mathbf{k}_{\parallel}, \omega) = \frac{2\pi}{|\mathbf{q}_{\parallel} + \mathbf{G}|} \sum_{m=-\infty}^{\infty} \int_{-d/2}^{d/2} n_{\mathbf{G}}(z', \mathbf{k}_{\parallel}, \omega) \times e^{-|\mathbf{k}_{\parallel} + \mathbf{G}||z - z' - mL|} dz' \quad (\text{A1})$$

created by $n_{\mathbf{G}}(z, \mathbf{k}_{\parallel}, \omega)$ can be approximated separately for $m = 0$, i.e., the potential created by the induced density in the central layer (placed at $z = 0$), and $m \neq 0$, the potential created by all other layers. Here, L is the layer distance (supercell height) and d the “physical” width of the layer. Obviously, d is not uniquely defined. We will see later that d cancels in the final result.

For the approximation, we consider z in the central layer, so $|z - z'|$ is always small (and smaller than L). With $e^{-|\mathbf{k}_{\parallel} + \mathbf{G}||z - z'|} \approx 1$ and $\cosh(|\mathbf{k}_{\parallel} + \mathbf{G}||z - z'|) \approx 1$, this yields an approximate z -independent induced potential in the layer

$$U_{\mathbf{G}}^{\text{ind}}(\mathbf{k}_{\parallel}, \omega) = \frac{2\pi d}{|\mathbf{k}_{\parallel} + \mathbf{G}|} \left(1 + \frac{2}{e^{|\mathbf{k}_{\parallel} + \mathbf{G}|L} - 1} \right) \bar{n}_{\mathbf{G}}(\mathbf{k}_{\parallel}, \omega) \quad (\text{A2})$$

with $\bar{n}_{\mathbf{G}}(\mathbf{k}_{\parallel}, \omega) = \frac{1}{d} \int_{-d/2}^{d/2} n_{\mathbf{G}}(z', \mathbf{k}_{\parallel}, \omega) dz'$, the induced charge averaged over the layer thickness.

The inverse dielectric function in the layer is

$$\begin{aligned} \varepsilon^{-1}(\mathbf{k}_{\parallel}, \omega; L) &= \frac{\delta[U_0^{\text{ext}}(\mathbf{k}_{\parallel}, \omega) + U_0^{\text{ind}}(\mathbf{k}_{\parallel}, \omega)]}{\delta U_0^{\text{ext}}(\mathbf{k}_{\parallel}, \omega)} \\ &= 1 + \frac{2\pi d}{k_{\parallel}} \left(1 + \frac{2}{e^{k_{\parallel}L} - 1} \right) \bar{R}(\mathbf{k}_{\parallel}, \omega; L) \end{aligned} \quad (\text{A3})$$

with the renormalized response function $\bar{R}(\mathbf{k}_{\parallel}, \omega; L) = \delta \bar{n}_0(\mathbf{k}_{\parallel}, \omega; L) / \delta U_0^{\text{ext}}(\mathbf{k}_{\parallel}, \omega)$ averaged over the layer. Here, we restrict ourselves to the Fourier components $\mathbf{G} = \mathbf{0}$. From now on, we denote the L dependence explicitly.

The averaged response function can be expressed as

$$\bar{R}(\mathbf{k}_{\parallel}, \omega; L) = \varepsilon^{-1}(\mathbf{k}_{\parallel}, \omega; L) P(\mathbf{k}_{\parallel}, \omega), \quad (\text{A4})$$

where it has been used that the polarizability $P(\mathbf{k}_{\parallel}, \omega)$ should, to a good approximation, be independent of the layer distance.

Plugging this into Eq. (A3) leads to

$$\varepsilon^{-1}(\mathbf{k}_{\parallel}, \omega; L) = \left[1 - \frac{2\pi d}{k_{\parallel}} \left(1 + \frac{2}{e^{k_{\parallel}L} - 1} \right) P(\mathbf{k}_{\parallel}, \omega) \right]^{-1}. \quad (\text{A5})$$

From RPA, we can obtain the head element of the inverse 3D dielectric function

$$\varepsilon_{00}^{-1}(\mathbf{k}_{\parallel}, \omega; L) = 1 + \frac{4\pi}{k_{\parallel}^2} R_{00}(\mathbf{k}_{\parallel}, \omega; L) \quad (\text{A6})$$

with the head of the 3D renormalized response function $R_{00}(\mathbf{k}_{\parallel}, \omega; L)$, which equals $\frac{d}{L} \bar{R}(\mathbf{k}_{\parallel}, \omega; L)$. Combining Eqs. (A4)–(A6) yields

$$-\lim_{L \rightarrow \infty} L \text{Im} \varepsilon_{00}^{-1}(\mathbf{k}_{\parallel}, \omega; L) = -\frac{4\pi d}{k_{\parallel}^2} \text{Im} \frac{P(\mathbf{k}_{\parallel}, \omega)}{1 - \frac{2\pi d}{k_{\parallel}} P(\mathbf{k}_{\parallel}, \omega)}, \quad (\text{A7})$$

for the imaginary part of the L -scaled supercell limit, which we now write in terms of the known function $\varepsilon_{00}^{-1}(\mathbf{k}_{\parallel}, \omega; L)$. To this end, we again employ Eqs. (A4)–(A6) to express $P(\mathbf{k}_{\parallel}, \omega)$ with the help of $\varepsilon_{00}^{-1}(\mathbf{k}_{\parallel}, \omega; L)$, which finally gives Eq. (23).

-
- [1] J. Hillier and R. F. Baker, *J. Appl. Phys.* **15**, 663 (1944).
[2] P. Schattschneider, *Fundamentals of Inelastic Electron Scattering* (Springer, Vienna, 1986), pp. 95–96.
[3] W. Grogger, F. Hofer, G. Kothleitner, and B. Schaffer, *Top. Catal.* **50**, 200 (2008).
[4] R. Egerton, *Ultramicroscopy* **107**, 575 (2007).
[5] H. C. Nerl, K. T. Winther, F. S. Hage, K. S. Thygesen, L. Houben, C. Backes, J. N. Coleman, Q. M. Ramasse, and V. Nicolosi, *npj 2D Mater Appl* **1**, 2 (2017).
[6] P. Wachsmuth, R. Hambach, M. K. Kinyanjui, M. Guzzo, G. Benner, and U. Kaiser, *Phys. Rev. B* **88**, 075433 (2013).
[7] P. Nozières and D. Pines, *Phys. Rev.* **113**, 1254 (1959).
[8] R. Egerton, *Electron Energy-Loss Spectroscopy in the Electron Microscope* (Springer, Boston, 2011).
[9] N. Onofrio, D. Guzman, and A. Strachan, *J. Appl. Phys.* **122**, 185102 (2017).
[10] V. Carozo, Y. Wang, K. Fujisawa, B. R. Carvalho, A. McCreary, S. Feng, Z. Lin, C. Zhou, N. Perea-López, A. L. Elías, B. Kabius, V. H. Crespi, and M. Terrones, *Sci. Adv.* **3**, e1602813 (2017).
[11] S. Ismail-Beigi, *Phys. Rev. B* **73**, 233103 (2006).
[12] F. Hüser, T. Olsen, and K. S. Thygesen, *Phys. Rev. B* **88**, 245309 (2013).
[13] D. Y. Qiu, F. H. da Jornada, and S. G. Louie, *Phys. Rev. Lett.* **115**, 119901(E) (2015).
[14] C. Freysoldt, P. Eggert, P. Rinke, A. Schindlmayr, and M. Scheffler, *Phys. Rev. B* **77**, 235428 (2008).
[15] N. Tancogne-Dejean, C. Giorgetti, and V. Véniard, *Phys. Rev. B* **92**, 245308 (2015).
[16] C. Giorgetti, I. Iagupov, and V. Véniard, *Phys. Rev. B* **101**, 035431 (2020).
[17] V. U. Nazarov, F. Alharbi, T. S. Fisher, and S. Kais, *Phys. Rev. B* **89**, 195423 (2014).
[18] V. U. Nazarov, E. E. Krasovskii, and V. M. Silkin, in *Springer Handbook of Surface Science*, edited by M. Rocca, T. S. Rahman, and L. Vattuone (Springer International Publishing, Cham, 2020), pp. 501–530.
[19] E. Runge and E. K. U. Gross, *Phys. Rev. Lett.* **52**, 997 (1984).
[20] M. Petersilka, U. J. Gossmann, and E. K. U. Gross, *Phys. Rev. Lett.* **76**, 1212 (1996).
[21] S. L. Adler, *Phys. Rev.* **126**, 413 (1962).
[22] N. Wiser, *Phys. Rev.* **129**, 62 (1963).
[23] S. Botti, A. Schindlmayr, R. Del Sole, and L. Reining, *Rep. Prog. Phys.* **70**, 357 (2007).
[24] C. Friedrich, S. Blügel, and A. Schindlmayr, *Phys. Rev. B* **81**, 125102 (2010). **104**, 039901 (2021).
[25] R. Hambach, Theory and ab-initio calculations of collective excitations in nanostructures: Towards spatially-resolved EELS, Ph.D. thesis, Ecole Polytechnique Palaiseau, 2010.
[26] D. Aspnes, *Thin Solid Films* **89**, 249 (1982).
[27] Further details available from <http://www.flapw.de>.
[28] J. P. Perdew, K. Burke, and M. Ernzerhof, *Phys. Rev. Lett.* **77**, 3865 (1996).
[29] R. G. Dickinson and L. Pauling, *J. Am. Chem. Soc.* **45**, 1466 (1923).
[30] E. Budak and Ç. Bozkurt, *Phys. B: Condens. Matter* **405**, 4702 (2010).
[31] L. Boulet-Roblin, D. Sheptyakov, P. Borel, C. Tessier, P. Novák, and C. Vilevieille, *J. Mater. Chem. A* **5**, 25574 (2017).
[32] A. Molina-Sánchez, K. Hummer, and L. Wirtz, *Surf. Sci. Rep.* **70**, 554 (2015).
[33] J. Rath and A. J. Freeman, *Phys. Rev. B* **11**, 2109 (1975).
[34] E. Moynihan, S. Rost, E. O’Connell, Q. Ramasse, C. Friedrich, and U. Bangert, *J. Microsc.* **279**, 256 (2020).
[35] C. T. Pan, R. R. Nair, U. Bangert, Q. Ramasse, R. Jalil, R. Zan, C. R. Seabourne, and A. J. Scott, *Phys. Rev. B* **85**, 045440 (2012).
[36] C. Elias, P. Valvin, T. Pelini, A. Summerfield, C. J. Mellor, T. S. Cheng, L. Eaves, C. T. Foxon, P. H. Beton, S. V. Novikov, B. Gil, and G. Cassabois, *Nat. Commun.* **10**, 2639 (2019).
[37] J. C. Idrobo and W. Zhou, *Ultramicroscopy* **180**, 156 (2017).
[38] V. Nazarov, *New J. Phys.* **17**, 073018 (2015).